The Astrophysical Journal, 926:112 (15pp), 2022 February 20 https://doi.org/10.3847/1538-4357/ac4506

Radio and X-Ray Observations of the Luminous Fast Blue Optical Transient AT 2020xnd

Joe S. Bright[1,2], Raffaella Margutti[1,2], David Matthews[1,2], Daniel Brethauer[1,2], Deanne Coppejans[2,3], Mark H. Wieringa[4], Brian D. Metzger[5,6], Lindsay DeMarchi[2], Tanmoy Laskar[7,8], Charles Romero[9,10,11], Kate D. Alexander[2], Assaf Horesh[12], Giulia Migliori[13], Ryan Chornock[1], E. Berger[9], Michael Bietenholz[14,15], Mark J. Devlin[11], Simon R. Dicker[11], W. V. Jacobson-Galán[1,2], Brian S. Mason[16], Dan Milisavljevic[17], Sara E. Motta[18,19], Tony Mroczkowski[20], Enrico Ramirez-Ruiz[21,22], Lauren Rhodes[19,23], Craig L. Sarazin[24], Itai Sfaradi[12], and Jonathan Sievers[25]

[1] Department of Astronomy, University of California, Berkeley, CA 94720-3411, USA; joe.bright@berkeley.edu
[2] Center for Interdisciplinary Exploration and Research in Astrophysics (CIERA) and Department of Physics and Astronomy, Northwestern University, Evanston, IL 60208, USA
[3] Department of Physics, University of Warwick, Coventry CV4 7AL, UK
[4] CSIRO Space & Astronomy, PO Box 76, Epping, NSW 1710, Australia
[5] Department of Physics and Columbia Astrophysics Laboratory, Columbia University, Pupin Hall, New York, NY 10027, USA
[6] Center for Computational Astrophysics, Flatiron Institute, 162 5th Ave, New York, NY 10010, USA
[7] Department of Physics, University of Bath, Claverton Down, Bath BA2 7AY, UK
[8] Department of Astrophysics/IMAPP, Radboud University Nijmegen, P.O. Box 9010, 6500 GL Nijmegen, The Netherlands
[9] Center for Astrophysics | Harvard & Smithsonian, Cambridge, MA 02138, USA
[10] Green Bank Observatory, P.O. Box 2, Green Bank, WV 24944, USA
[11] Department of Physics and Astronomy, University of Pennsylvania, 209 South 33rd Street, Philadelphia, PA 19104, USA
[12] Racah Institute of Physics, The Hebrew University of Jerusalem, Jerusalem 91904, Israel
[13] Istituto di Radioastronomia—INAF, Via P. Gobetti 101, I-40129 Bologna, Italy
[14] Department of Physics and Astronomy, York University, Toronto, M3J 1P3, Ontario, Canada
[15] SARAO/Hartebeesthoek Radio Observatory, PO Box 443, Krugersdorp, 1740, South Africa
[16] National Radio Astronomy Observatory, 520 Edgemont Rd., Charlottesville, VA 22903, USA
[17] Department of Physics and Astronomy, Purdue University, 525 Northwestern Avenue, West Lafayette, IN 47907, USA
[18] Istituto Nazionale di Astrofisica, Osservatorio Astronomico di Brera, via E. Bianchi 46, 23807 Merate (LC), Italy
[19] Department of Physics, Astrophysics, University of Oxford, Denys Wilkinson Building, Keble Road, Oxford OX1 3RH, UK
[20] ESO—European Southern Observatory, Karl-Schwarzschild-Str. 2, D-85748 Garching b. München, Germany
[21] Department of Astronomy and Astrophysics, University of California, Santa Cruz, CA 95064, USA
[22] Niels Bohr Institute, University of Copenhagen, Blegdamsvej 17, DK-2100 Copenhagen, Denmark
[23] Max Planck Institute für Radioastronomie, Auf dem Hügel, Bonn D-53121, Germany
[24] Department of Astronomy, University of Virginia, 530 McCormick Road, Charlottesville, VA 22904-4325, USA
[25] Department of Physics, McGill University, 3600 University Street, Montreal, QC H3A 2T8, Canada
Received 2021 October 11; revised 2021 November 22; accepted 2021 November 22; published 2022 February 17

Abstract

We present deep X-ray and radio observations of the fast blue optical transient (FBOT) AT 2020xnd/ZTF 20acigmel at $z = 0.2433$ from 13 days to 269 days after explosion. AT 2020xnd belongs to the category of optically luminous FBOTs with similarities to the archetypal event AT 2018cow. AT 2020xnd shows luminous radio emission reaching $L_\nu \approx 8 \times 10^{29}$ erg s^{-1} Hz^{-1} at 20 GHz and 75 days post-explosion, accompanied by luminous and rapidly fading soft X-ray emission peaking at $L_X \approx 6 \times 10^{42}$ erg s^{-1}. Interpreting the radio emission in the context of synchrotron radiation from the explosion's shock interaction with the environment, we find that AT 2020xnd launched a high-velocity outflow ($v \sim 0.1c$–$0.2c$) propagating into a dense circumstellar medium (effective $\dot{M} \approx 10^{-3}\, M_\odot$ yr^{-1} for an assumed wind velocity of $v_w = 1000$ km s^{-1}). Similar to AT 2018cow, the detected X-ray emission is in excess compared to the extrapolated synchrotron spectrum and constitutes a different emission component, possibly powered by accretion onto a newly formed black hole or neutron star. These properties make AT 2020xnd a high-redshift analog to AT 2018cow, and establish AT 2020xnd as the fourth member of the class of optically luminous FBOTs with luminous multiwavelength counterparts.

Unified Astronomy Thesaurus concepts: Radio transient sources (2008); Transient sources (1851); X-ray transient sources (1852); Supernovae (1668)

1. Introduction

The advent of wide-field and high-cadence optical transient surveys, along with real-time discovery efforts, has expanded the parameter space in the search for new classes of extragalactic transient with rapid evolution timescales. Observations from such surveys have revealed a variety of optical transients spending $\lesssim$10 days above half maximum brightness, atypical for the majority of extragalactic transients previously discovered (e.g., Kasliwal et al. 2010; Poznanski et al. 2010). Among these are the fast blue optical transients (FBOTs), characterized by their rapid rise to maximum light ($\lesssim$10 days), peak optical luminosity reaching $L_{pk} > 10^{43}$ erg s^{-1}, and persistently blue colors (e.g., Drout et al. 2014; Arcavi et al. 2016; Tanaka et al. 2016; Pursiainen et al. 2018;

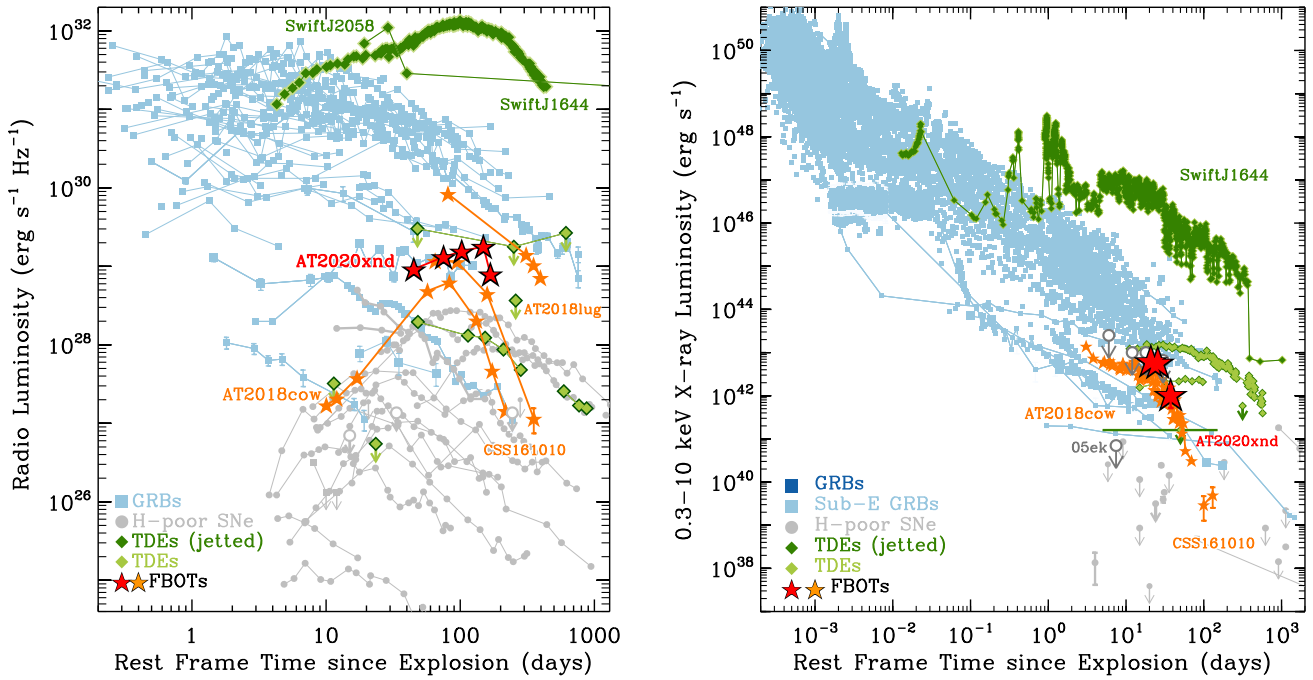

Figure 1. Left: the evolving radio luminosities of extragalactic H-poor explosive transients, including long GRBs (light blue squares), SNe (light gray circles), and TDEs (green diamonds) at $\nu \approx 5$ GHz. Like the other FBOTs (orange stars), AT 2020xnd (red stars) drops off rapidly at late times. Right: X-ray parameter space for the same set of transients. References: Margutti et al. (2019), Alexander et al. (2020), Coppejans et al. (2020), Ho et al. (2020c) and references therein.

Rest et al. 2018; Perley et al. 2020; Ho et al. 2021a). FBOTs appear to be intrinsically rare events, occurring at between 1% and 10% of the core-collapse supernova rate in the local universe (Li et al. 2011; Drout et al. 2014; Pursiainen et al. 2018; Tampo et al. 2020).

The most optically luminous FBOTs are further distinguished from other rapidly evolving extragalactic transients—such as subluminous Type IIb/Ib supernovae (SNe) (Poznanski et al. 2010; Ho et al. 2021a), luminous Type Ibn or hybrid IIn/Ibn SNe (Ho et al. 2021a), and Type IIn SNe (e.g., Ofek et al. 2010)—based on the presence of highly luminous X-ray and radio emission, which are comparable to those seen in short gamma-ray bursts (GRBs) and well in excess of what is seen in typical core-collapse SNe (e.g., Margutti et al. 2019; Bright et al. 2020a; Ho et al. 2020b, 2021b; Coppejans et al. 2020; Matthews et al. 2020, and see Figure 1). Although the population of FBOTs with associated high-energy emission remains small, FBOTs with luminous radio and X-ray emission are rarer still, occurring at $\lesssim$1% of the rate of core-collapse supernovae (CCSNe) below $z \sim 0.5$ (Ho et al. 2020b; Coppejans et al. 2020). In the optical, FBOTs do not show a ^{56}Ni-powered decay tail, do show high-temperature photospheric emission, and are preferentially located in dwarf galaxies (Coppejans et al. 2020; Perley et al. 2021).

The prototypical optically luminous FBOT with associated emission at X-ray and radio wavelengths is AT 2018cow (Prentice et al. 2018), which, at only $\sim$60 Mpc, was the subject of extended observing campaigns at centimeter, millimeter, and X-ray wavelengths (Rivera Sandoval et al. 2018; Ho et al. 2019a; Kuin et al. 2019; Margutti et al. 2019; Perley et al. 2019; Nayana & Chandra 2021). The radio observations revealed the presence of a shock with velocity of $\sim 0.1c$ interacting with a dense and asymmetric circumstellar medium (CSM), while the X-ray emission was in excess of an extrapolation of the radio spectrum. This X-ray excess suggested an additional emission component, which was interpreted as a central engine—an accreting compact object or a spin-powered magnetar. The X-ray spectrum of AT 2018cow also clearly contained multiple components, with an excess above $\sim$10 keV seen at early times that had vanished at $\sim$15 days post-explosion. The origin of this hard excess remains unclear; Margutti et al. (2019) interpreted it as a Compton hump feature resulting from X-rays interacting with a fast ejecta shell, or reflection off an accretion funnel. Both scenarios suggest an X-ray source embedded within the explosion. While X-ray observations of CSS 161010 (Coppejans et al. 2020) at $d \approx 150$ Mpc were not as comprehensive as for AT 2018cow, the former showed a similar excess relative to its well sampled radio spectral energy distributions (SEDs), suggesting that the presence of a central engine is a feature of the FBOTs (Margutti et al. 2019; Coppejans et al. 2020).

In this work we present radio and X-ray observations of the FBOT AT 2020xnd (ZTF 20acigmel), the third FBOT with both luminous X-ray and radio emission. Additional radio observations of AT 2020xnd/ZTF 20acigmel (including high-frequency monitoring with the SMA/NOEMA) were obtained by an independent observing team and are presented in Ho et al. (2021a). AT 2020xnd was discovered on 2020 October 12 by the Zwicky Transient Facility (ZTF, Bellm et al. 2019; Graham et al. 2019) as part of the two-day cadence public survey (Perley et al. 2021). Follow-up observations identified a candidate (dwarf) host galaxy at $z = 0.2433$. Based on the rapid rise and decay, the blue color, the dwarf galaxy host, and the high optical luminosity of this source, Perley et al. (2021) classified AT 2020xnd as an FBOT.

Upon the announcement that AT 2020xnd was producing luminous radio emission (Ho et al. 2020a, 2021b), we initiated a multiwavelength observing campaign on the target beginning at 15 days post-discovery. Our campaign included observations at radio (AMI-LA, ATCA, eMERLIN, GMRT, MeerKAT, VLA), submillimeter/millimeter (ALMA, GBT), and X-ray (Chandra,

XMM-Newton) frequencies. We particularly highlight the use of the MUSTANG-2 bolometer camera on the GBT, which provided us with early-time millimeter data, demonstrating its suitability for rapid transient follow-up at high frequencies.

We structure the rest of this manuscript as follows. In Section 2 we describe our observations and the data reduction process. In Section 3 we derive and present the results for our analysis of our radio and X-ray observations. Finally, in Section 4 and Section 5 we discuss our results and give our conclusions, respectively.

2. Observations

Throughout this paper, measurements in time are in reference to the explosion date (T_0), which is MJD 59,132.0 (Perley et al. 2021), and are in the observed frame, unless otherwise specified. Uncertainties are reported at the 1σ (Gaussian equivalent) confidence level (c.l.) and upper limits at the 3σ c.l. unless explicitly noted. We adopt standard ΛCDM cosmology with $H_0 = 69.6\,\mathrm{km\,s^{-1}\,Mpc^{-1}}$, $\Omega_\mathrm{M} = 0.286$, and $\Omega_\Lambda = 0.714$ (Bennett et al. 2014). At $z = 0.2433$ (Perley et al. 2021) the luminosity distance of AT 2020xnd is $D_L = 1\,232$ Mpc and the angular diameter distance is $D_\theta = 797$ Mpc.

2.1. Radio

In this section we describe our large radio campaign on AT 2020xnd. A summary of all of our radio observations is given in Table 1. The calibrators used and array configurations are given in Table 2.

2.1.1. Australia Telescope Compact Array

The field of AT 2020xnd was observed with the Australia Telescope Compact Array (ATCA) under project codes CX471 (PI Bright) and CX472 (PI Ho), beginning on 2020 October 25 ($T_0 + 15$ days). Data were recorded with either the 4 cm receiver (which collects data simultaneously at 5.5 and 9 GHz), the 15 mm receiver (which collects data simultaneously at 17 and 19 GHz), or the 7 mm receiver (which collects data simultaneously at 33 and 35 GHz). Each frequency was observed with a 2 GHz bandwidth and processed by the Compact Array Broadband Backend (CABB; Wilson et al. 2011). Data taken as part of CX471 were reduced and imaged in MIRIAD (Sault et al. 1995) using standard techniques. Data from CX472 are reported in Dobie et al. (2020a, 2020b, 2020c). For observations taken with the 15 mm or 7 mm receiver the subbands were jointly imaged in order to double the bandwidth and increase image sensitivity.

2.1.2. Karl G. Jansky Very Large Array

We initiated Karl G. Jansky Very Large Array (VLA) observations of AT 2020xnd as part of program VLA/20A-354 (PI Margutti) beginning on 2020 November 5 (MJD 59,158, $T_0 + 26$ days). Observations were taken at *S*-, *C*-, *X*-, *Ku*-, *K*-, and *Ka*-bands, utilizing the WIDAR correlator, with a 2 GHz bandwidth at *S*-band, a 4 GHz bandwidth at *C*- and *X*-bands, a 6 GHz bandwidth at *Ku*-band, and an 8 GHz bandwidth at *K*-band and *Ka*-band. AT 2020xnd lies in the decl. range of the Clarke satellite belt as observed from the VLA, and as such we shifted the basebands at *C*- and *X*-bands to reduce the impact of radio-frequency interference. Data were reduced with the VLA CASA (McMullin et al. 2007) calibration pipeline version 2020.1.0.36 and then manually inspected, further flagged, and reprocessed through the pipeline. The final imaging was performed using WSClean (Offringa et al. 2014; Offringa & Smirnov 2017), where we used -FIT-SPECTRAL-POL = 2 (equivalent to using two Taylor terms when using CASA) to account for the wide fractional bandwidth of the VLA. Images were created using a Briggs parameter between 0 and 1 depending on the array configuration. Where we measured the flux within small subbands of the bandwidth we set -NO-MF-WEIGHTING in order to avoid the creation of artificial spectral structure. Fitting was performed using PYBDSF (Mohan & Rafferty 2015) with the size of the source fixed to that of the synthesized beam.

2.1.3. Enhanced Multi-element Radio Linked Interferometer Network

We were awarded DDT observations (project ID DD10005, PI Bright) of AT 2020xnd with the Enhanced Multi-Element Radio Linked Interferometer Network (eMERLIN) and observed the field of AT 2020xnd on 2020 November 6 ($T_0 + 27$ days). Observations were conducted at a central frequency of 5.075 GHz with a 512 GHz bandwidth. The Lovell telescope was not included in the array. Data calibration was performed with the eMERLIN CASA pipeline using standard techniques. We did not detect emission consistent with the position of AT 2020xnd. We triggered a further four *C*-band observations as part of project ID CY11008 (PI Bright). Further observations were reduced using the same strategy, with imaging performed manually on the pipeline output, and we detected the source in one epoch at $T_0 + 102$ days.

2.1.4. Robert C. Byrd Green Bank Telescope

We observed AT 2020xnd with the Robert C. Byrd Green Bank Telescope (GBT) with the MUSTANG-2 instrument (Dicker et al. 2014) beginning on $T_0 + 28$ days (MJD 59,160). Data were taken under projects GBT20B_437 (PI Bright) and GBT20B_440 (PI Bright). MUSTANG-2 is a bolometer camera providing 9″ resolution and high continuum sensitivity between 75 and 105 GHz. Due to the wide bandwidth that MUSTANG-2 is sensitive to, the effective central frequency of any given observation depends on the spectral index of the source being observed. The spectral index from AT 2020xnd (as determined by our modeling in Section 3) is between ∼1.5 and 0 through the MUSTANG-2 bandpass, which results in a central frequency between 88.6 and 88.9 GHz. We therefore use 90 GHz as the central frequency, and do not consider the small shift due to spectral index. The MUSTANG-2 data are reduced via the MIDAS pipeline, which is described in Romero et al. (2020). The MIDAS pipeline relies on Fourier filtering the data and subtraction of principal components (via principal component analysis). For point sources such as AT 2020xnd the recovered flux density is insensitive to the range of typical filtering parameters used. We used six principal components and a notched Fourier filter, keeping frequencies between 0.07 and 41 Hz. The MUSTANG-2 data were flux-calibrated relative to Neptune, and a nearby secondary calibrator (a point source) was used to track pointing and gain shifts during each night. The observations of the secondary calibrators were also used to determine the beam size for each night.

Table 1
Radio Observations of AT 2020xnd

Start Date (dd/mm/yy)	Centroid MJD	Phase[a] (day)	Frequency (GHz)	Bandwidth (GHz)	Flux Density[b] (μJy)	Facility
22/10/20	59,145.01	13.01	10	4	23 ± 5	VLA
25/10/20	59,147.28	15.28	5.5	2	<60	ATCA
25/10/20	59,147.28	15.28	9	2	<50	ATCA
29/10/20	59,151.41	19.41	18	4	110 ± 20	ATCA
05/11/20	59,158.22	26.22	19.09	2	192 ± 32	VLA
05/11/20	59,158.22	26.22	21.07	2	209 ± 37	VLA
05/11/20	59,158.22	26.22	23.05	2	273 ± 41	VLA
05/11/20	59,158.22	26.22	25.03	2	269 ± 35	VLA
05/11/20	59,158.74	26.74	13.49	3	122 ± 15	VLA
05/11/20	59,158.74	26.74	16.51	3	139 ± 16	VLA
06/11/20	59,159.82	27.82	5.07	0.512	<54	eMERLIN
07/11/20	59,160.09	28.09	90.00[c]	30	900 ± 100	GBT
07/11/20	59,160.41	28.41	34	4	310 ± 20	ATCA
16/11/20	59,169.11	37.11	18.98	2	304 ± 31	VLA
16/11/20	59,169.11	37.11	20.99	2	350 ± 31	VLA
16/11/20	59,169.11	37.11	23.01	2	399 ± 32	VLA
16/11/20	59,169.11	37.11	25.02	2	433 ± 33	VLA
16/11/20	59,169.14	37.14	12.97	2	200 ± 23	VLA
16/11/20	59,169.14	37.14	15.00	2	213 ± 17	VLA
16/11/20	59,169.14	37.14	17.02	2	262 ± 23	VLA
19/11/20	59,172.27	40.27	18	4	240 ± 31	ATCA
24/11/20	59,177.09	45.09	9.82	4	112 ± 15	VLA
24/11/20	59,177.10	45.10	6.22	4	51 ± 12	VLA
25/11/20	59,178.06	46.06	90.00[c]	30	560 ± 60	GBT
27/11/20	59,180.25	48.24	34	4	490 ± 63	ATCA
03/12/20	59,186.05	54.05	90.00[c]	30	360 ± 60	GBT
15/12/20	59,198.59	66.59	5.072	0.512	<114	eMERLIN
24/12/20	59,207.05	75.05	29.98	2	451 ± 51	VLA
24/12/20	59,207.05	75.05	31.99	2	480 ± 58	VLA
24/12/20	59,207.05	75.05	34.01	2	471 ± 52	VLA
24/12/20	59,207.05	75.05	36.02	2	451 ± 60	VLA
24/12/20	59,207.07	75.07	18.98	2	420 ± 33	VLA
24/12/20	59,207.07	75.07	20.99	2	435 ± 34	VLA
24/12/20	59,207.07	75.07	23.01	2	444 ± 36	VLA
24/12/20	59,207.07	75.07	25.02	2	444 ± 34	VLA
24/12/20	59,207.09	75.09	12.98	2	278 ± 24	VLA
24/12/20	59,207.09	75.09	15.00	2	317 ± 23	VLA
24/12/20	59,207.09	75.09	17.02	2	331 ± 25	VLA
24/12/20	59,207.11	75.11	3	2	73 ± 18	VLA
26/12/20	59,209.26	77.26	18	4	252 ± 36	ATCA
19/01/21	59,234.61	102.61	5.072	0.512	86 ± 19	eMERLIN
09/02/21	59,254.36	122.36	1.25	0.4	<87	GMRT
07/03/21	59,280.69	148.69	33	8	<72	VLA
07/03/21	59,280.71	148.71	22	8	70 ± 17	VLA
07/03/21	59,280.73	148.73	15	6	90 ± 12	VLA
07/03/21	59,280.75	148.75	6.224	4	99 ± 16	VLA
18/03/21	59,291.44	159.44	15.5	4	<156	AMI-LA
21/03/21	59,294.33	162.33	0.75	0.4	<177	GMRT
23/03/21	59,296.33	164.33	1.26	0.4	<75	GMRT
26/03/21	59,299.77	167.77	3	2	<105	VLA
26/03/21	59,299.78	167.78	9.824	4	49 ± 19	VLA
26/03/21	59,264.80	167.80	6.224	4	44 ± 22	VLA
12/04/21	59,316.48	184.48	97.49	8	<42	ALMA
12/04/21	59,316.53	184.53	144.99	8	<45	ALMA
16/03/21	59,323.94	191.94	15.5	4	<135	AMI-LA
19/04/21	59,323.18	191.18	1.28	0.856	<60	MeerKAT
23/04/21	59,327.28	195.28	5.072	0.512	<60	eMERLIN
29/05/21	59,363.33	231.33	1.28	0.856	<48	MeerKAT
06/07/21	59,401.31	269.31	97.44	8	<18	ALMA

Notes.
[a] Days since MJD 59132, using the central time of the exposure on source.
[b] Uncertainties are quoted at 1σ, and upper limits are quoted at 3σ. The errors take a systematic uncertainty of 5% (VLA), 15% (GMRT), 10% (ATCA), 10% (eMERLIN), 10% (GBT), and 10% (MeerKAT) into account.
[c] As MUSTANG-2 is a bolometer instrument sensitive between 75 and 105 GHz the central frequency depends on the spectral index of the emission through the band. The impact of this is discussed in further detail in the main text.

Table 2
Calibrators and Array Configurations Used during Our Radio Observations of AT 2020xnd

Instrument	Primary Calibrator(s)	Secondary/Pointing Calibrator(s)	Array Configuration(s)
ALMA	J2253+1608	J2218−0335	C-5, C-7
AMI-LA	3C286	J2226+0052	fixed
ATCA	1934−638	2216−038	6B, H168
eMERLIN	1331+3030	1407+2827, 2218−0335	fixed
GBT	Neptune	2225−0457	single dish
GMRT	3C48	J2212+0152	fixed
MeerKAT	J1939−6342	J2225−0457	fixed
VLA	3C147, 3C48	J2218−0335, J2225−0457	A, BnA, D

2.1.5. Giant Metrewave Radio Telescope

We observed the field of AT 2020xnd with the Giant Metrewave Radio Telescope (GMRT) beginning on $T_0 + 162$ days at 0.75 GHz and 1.25 GHz, under program 39_034 (PI Matthews). The data were reduced manually using standard calibration techniques, with multiple rounds of phase-only and then amplitude and phase self-calibration performed. We then performed a single round of direction-dependent self-calibration using killMS (Tasse 2014; Smirnov & Tasse 2015) to solve for direction-dependent gains and DDFacet (Tasse et al. 2018) to perform imaging and create a compatible sky model.

2.1.6. MeerKAT

We observed the field of AT 2020xnd with the MeerKAT radio telescope as part of project SCI-20210212-JB-01 (PI Bright) starting at $T_0 + 191$ days. Observations were taken at a central frequency of 1.28 GHz with a bandwidth of 856 MHz and the correlator in 4k mode (4096 spectral channels of width 209 kHz). Observations were reduced using the OXKAT[26] reduction pipeline (McMullin et al. 2007; Offringa et al. 2014; Kurtzer et al. 2017; Kenyon et al. 2018; Heywood 2020), which is a set of semiautomated scripts that we use to perform phase-reference calibration and self-calibration.

2.1.7. Atacama Large Millimeter/submillimeter Array

Due to the COVID-19 pandemic we were not able to trigger Atacama Large Millimeter/submillimeter Array (ALMA) observations close to T_0; however, we obtained late-time observations of AT 2020xnd under project code 2019.1.01157.T (PI Coppejans) at $T_0 + 184$ days and $T_0 + 269$ days (Table 1). The first epoch consisted of a band-3 and a band-4 observation, whereas the second epoch consisted of a single deep band-3 observation. We used the results of the ALMA pipeline (which uses standard techniques and the CASA package) to calibrate and image the data. AT 2020xnd was not detected in any of our ALMA observations.

2.1.8. Arcminute Microkelvin Imager Large Array

We observed the field of AT 2020xnd with the Arcminute Microkelvin Imager Large Array (AMI-LA; Zwart et al. 2008; Hickish et al. 2018) (PI Bright) beginning on $T_0 + 154$ days. We observed the field on a further three occasions but did not detect emission from AT 2020xnd. Data were reduced using standard techniques with the REDUCE_DC software (e.g., Perrott et al. 2013; Bright et al. 2019).

[26] https://github.com/IanHeywood/oxkat

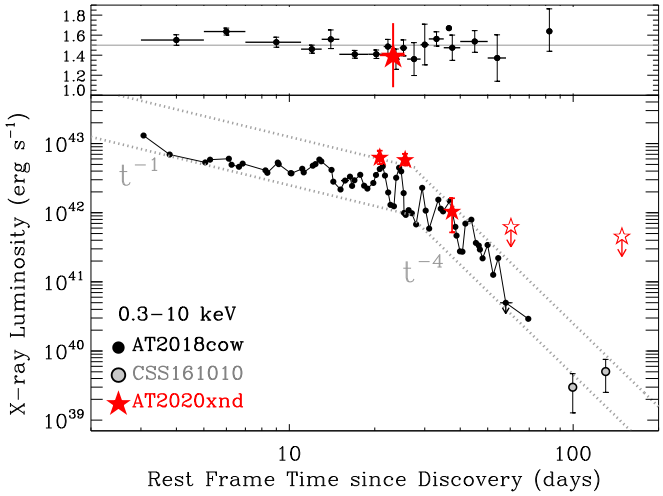

Figure 2. Main panel: soft X-ray (0.3-10 keV) luminosity evolution of AT 2020xnd (red stars) compared to the other two known FBOTs with X-ray detections, AT 2018cow and CSS 161010 (filled black and gray circles, respectively; Margutti et al. 2019; Coppejans et al. 2020). Dotted lines mark $L_X \propto t^{-1}$ and $L_X \propto t^{-4}$ power-law decays to guide the eye. Interestingly, AT 2020xnd shows a similar luminosity to AT 2018cow and seems to follow a similar, peculiar temporal evolution, with roughly constant X-ray flux at $\delta t \leqslant 30$ days followed by a sharp decay. Upper panel: evolution of spectral photon index with time for AT 2018cow and AT 2020xnd. The solid horizontal line is a photon index of 1.5.

2.2. X-Ray Observations

The broadband X-ray monitoring campaign described in this paper covered the time window $\delta t \sim 25$–240 days after explosion (Figure 2).

2.2.1. Chandra X-Ray Observatory (0.3–10 keV)

We acquired deep X-ray observations of AT 2020xnd with the Chandra X-ray Observatory (CXO) under a joint CXO–NuSTAR program #22500192 (PI Matthews; IDs 23547, 23548, 23549; exposure time of ≈19.8 ks per ID) covering the time period $\delta t = 25$–240 days. We reduced the ACIS-S data with the CIAO software package (v4.12) and relative calibration files (CALDB 4.9.3), applying standard ACIS data filtering (Fruscione et al. 2006).

We refined the CXO absolute astrometry by cross-matching the 0.5–8 keV X-ray sources blindly detected with wavdetect with optical sources in Sloan Digital Sky Survey DR9. After the realignment we find evidence for statistically significant X-ray emission at coordinates R.A. $= 22^h20^m02^s.036 \pm 0^s.078$ and $\delta = -02°50'25''.34 \pm 0''.11$, which is consistent with the optical and radio position of AT 2020xnd. The measured source count rates and the detection significance are reported in Table 3. At $\delta t_{\rm rest} < 25.6$ days (rest frame) the X-ray source shows roughly constant flux. The source experienced significant fading at $\delta t_{\rm rest} \geqslant 26$ days, and the flux decays as $F_X \propto t^{-\alpha}$ with $\alpha \approx 4.5$ (Figure 2). This very steep late-time X-ray flux decay is similar to that of AT 2018cow (Figure 2), which is the only other FBOT with X-ray observations at these epochs (Rivera Sandoval et al. 2018; Margutti et al. 2019). These properties make AT 2020xnd the third FBOT with luminous X-ray emission $L_X > 10^{42}$ erg s^{-1}

Table 3
Chandra X-Ray Observations of AT 2020xnd

Start Date (UT)	Phase[a] (days)	Exposure (ks)	Net Count Rate (0.5–8 keV) (10^{-4} counts s^{-1})	Significance (σ)	Flux[b] (0.3–10 keV) (10^{-14} erg s^{-1} cm^{-2})	Luminosity (0.3–10 keV) (10^{42} erg s^{-1})[c]
2020-11-04 15:51:28	25.9	19.82	12.2 ± 2.5	10.8[d]	$3.32^{+0.73}_{-0.75}$	$6.41^{+1.44}_{-1.41}$
2020-11-10 17:06:55	31.8	19.82	11.6 ± 2.5	9.9[d]	$3.26^{+0.81}_{-0.77}$	$6.29^{+1.45}_{-1.61}$
2020-11-25 22:55:07	46.6	19.82	1.95 ± 1.00	4.4[e]	$0.55^{+0.28}_{-0.28}$	$1.05^{+0.55}_{-0.55}$
2020-12-24 02:21:05	75.0	19.75	<1.52	<3	<0.33[f]	<0.60
2021-04-12 14:05:14	184.6	16.86	}<1.09[g]	<3	<0.24[f]	<0.43
2021-04-13 02:16:12	185.1	19.82				
2021-06-07 04:27:03	240.2	39.55	<0.76	<3	<0.17	<0.30

Notes.
[a] Days since MJD 59,132, using the middle time of the exposure.
[b] Uncertainties are quoted at 1σ, and upper limits are quoted at 3σ.
[c] Corrected for Galactic absorption.
[d] Blind-detection significance.
[e] Targeted-detection significance.
[f] A power-law spectral model with $\Gamma = 1.4$ is used to convert upper limits from count rates to fluxes.
[g] Exposures are merged for a deeper detection limit.

Table 4
NuSTAR X-Ray Upper Limits of AT 2020xnd

Start Date (UT)	Phase[a] (days)	Exposure[c] (ks)	Net Count Rate[c] (3–79 keV) (10^{-4} counts s^{-1})	Observed Flux[c] (3–79 keV) (10^{-14} erg s^{-1} cm^{-2})	Luminosity[c] (3–79 keV) (10^{42} erg s^{-1})
2020-11-04 05:06:09	25.2	57.73	<16.6	< 26.5	<48.5
2020-11-10 15:40:03	31.7	62.6	< 15.4	< 24.5	< 44.9
2020-11-30 22:00:05	51.9	81.8	< 13.9	< 22.2	< 40.6

Notes.
[a] Days since MJD 59,132.
[c] Exposure of Modules A plus exposure for Module B. We adopt a power-law spectral model with photon index $\Gamma = 1.5$ and a counts-to-flux factor of 1.5×10^{-10} (cgs units) for calculating upper limits.

(Figure 2) and the third with detected X-rays (Margutti et al. 2019; Coppejans et al. 2020).

For each of the first three CXO epochs we extracted a spectrum with `specextract` using a 1″ region around the X-ray source and a source-free region of 33″ for the background. The neutral hydrogen column density in the direction of the transient is $NH_{MW} = 4.8 \times 10^{20}\,cm^{-2}$ (Kalberla et al. 2005). We modeled each spectrum with an absorbed power-law model (`tbabs*ztbabs*pow` within `Xspec`; Arnaud 1996). We found no statistical evidence for spectral evolution. We thus proceeded with a joint spectral fit. The best-fitting power-law photon index is $\Gamma = 1.40^{+0.33}_{-0.32}$ and we place a 3σ limit on the intrinsic absorption column of $NH_{int} < 3 \times 10^{22}\,cm^{-2}$. The corresponding 0.3–10 keV fluxes and luminosities are reported in Table 3. We found no evidence for statistically significant X-ray emission at $\delta t_{rest} > 60$ days and we place upper limits on the source count rate of $\lesssim 10^{-4}$ counts s^{-1} (0.5–8 keV) assuming Poissonian statistics as appropriate in the regime of low count statistics. This leads to luminosity limits $L_X < (0.3\text{–}0.6) \times 10^{42}$ erg s^{-1} using the spectral parameters and model that best fit the earlier observations (Table 3).

2.2.2. NuSTAR (3–79 keV)

We observed AT 2020xnd using the Nuclear Spectroscopic Telescope Array (NuSTAR, 3–79 keV) under the joint CXO–NuSTAR program (PI Matthews; program 22500192; IDs 80701407002, 80701407004, 80701407006; Table 4). We reduced the data with `NuSTARDAS` (v1.9.2) and relative calibration files. We centered a source extraction aperture of 1′ at the CXO coordinates and we estimated the background using an annulus with inner and outer radii of 1.′1 and 3′, respectively. Using Poissonian statistics, we found no evidence for significant emission above the background in the source region. The resulting 3–79 keV count rate, flux, and luminosity limits are listed in Table 4. We adopt a power-law spectral model with photon index $\Gamma = 1.5$ and a counts-to-flux factor of 1.5×10^{-10} for the spectral calibration. We find $L_X < 5 \times 10^{43}$ erg s^{-1} (3–79 keV) in the time range probed by our observations, which corresponds to $\delta t_{rest} = T_0 + 25$ to $T_0 + 52$ days. For comparison, the hard X-ray Compton hump was detected in AT 2018cow with hard X-ray luminosities $\approx 10^{43}$ erg s^{-1} at $\delta t_{rest} < 15$ days (Margutti et al. 2019).

3. Results

3.1. General Considerations

AT 2020xnd shows a roughly constant X-ray luminosity at $\delta t_{rest} \leqslant 30$ days followed by a sharp decline, which was similarly seen in the FBOT AT 2018cow (Figure 2). Also shown in Figure 2 is the X-ray photon index of AT 2020xnd. The measured soft X-ray spectral index $\beta_x = 0.4^{+0.33}_{-0.34}$ (where $F_\nu \propto \nu^{-\beta_x}$, Section 2.2.1) is shallower than expected from

optically thin synchrotron emission above the cooling break frequency ν_c (Section 3.5). In this regime, $F_\nu \propto \nu^{-p/2}$ (e.g., Granot & Sari 2002), where p is the index of the power-law distribution of relativistic electrons with Lorentz factor γ_e ($N_e(\gamma_e) \propto \gamma_e^{-p}$). For relativistic shocks of long/short GRBs and the Newtonian shocks of SNe $p \approx 2$–3 (see, e.g., Chevalier & Fransson 2006; Fong et al. 2019), hence $F_\nu \propto \nu^{-\beta}$ with $\beta = 1$–1.5. This again is similar to what was seen in AT 2018cow (Margutti et al. 2019). While our NuSTAR observations probe the hard X-rays (3–79 keV), the large distance of AT 2020xnd only allows us to place upper limits in this region of the spectrum that are comparable to the luminosity of the observed Compton hump in AT 2018cow. However, since NuSTAR observations of AT 2020xnd started at $\delta t_{\rm rest} = 25$ days, which is after the Compton hump component faded away in AT 2018cow, we cannot rule out that AT 2020xnd exhibited a hard X-ray excess similar to the one seen in AT 2018cow at earlier times (Margutti et al. 2019).

Figure 3 shows the evolving radio SED of AT 2020xnd for different subsets of our radio data. At early times ($\delta t \lesssim T_0 + 30$ days) the emission is optically thick up to at least $\nu \sim 90$ GHz, with a spectral index of $\sim$1.4 below the break. The peak of the SED moves to lower flux density with time, while moving to a lower frequency, until we clearly see the peak in our data at $\delta t \approx T_0 + 75$ days. The optically thin spectral index is not constrained by our data. This spectral shape is similar to the one expected from self-absorbed synchrotron emission, albeit with a flatter self-absorption spectral index (which is expected to be $\sim$2 or $\sim$2.5). The evolution of the break and peak flux suggest the radio emission is from an evolving emitting region that expands and becomes optically thin to lower frequencies with time. This can be interpreted as the result of ejecta material from AT 2020xnd interacting with the CSM surrounding the progenitor. The flatter, optically thick slope that we measure could be the result of scintillation effects; however, we disfavor this due to the smoothness of the radio SEDs. We are unable to check for short-timescale variability or extreme in-band spectral indices (both features of scintillation) due to the low measured flux density of AT 2020xnd at low frequencies.

3.2. Modelling Radio SEDs

First, we focus on our radio observations at $\delta t \approx T_0 + 75$ days where the peak of the SED is best sampled. We employ the smoothed broken power-law SED model of Equation (1):

$$F(\nu, t) = F_p(t)\left[\left(\frac{\nu}{\nu_b(t)}\right)^{-b_1/s} + \left(\frac{\nu}{\nu_b(t)}\right)^{-b_2/s}\right]^{-s}, \quad (1)$$

where ν_b is the break frequency, F_p is the peak flux density at which the asymptotic power-law segments meet, $s > 0$ is a smoothing parameter, b_1 and b_2 are the optically thick and optically thin asymptotic spectral indices, respectively, at $\nu \ll \nu_b$ and $\nu \gg \nu_b$. Adopting $s = 1$ and $b_2 = -1$ as typically observed in SNe in the optically thin regime (Chevalier & Fransson 2006; although see Ho et al. (2021b) for a discussion of the possibility of a relativistic Maxwellian electron population being responsible for FBOT emission and causing a steeper post-break slope), we find $F_p = 960 \pm 70\ \mu$Jy and $\nu_b = 35 \pm 7$ GHz at $T_0 + 75$ days.[27]

[27] We use the Python module LMFIT for all fitting performed in this work.

Next we attempt to model the entire radio data set shown in Figure 3(b) assuming a power-law evolution in time of the break frequency ($\nu_b(t) = \nu_{b,0}(t/T_0)^{-\alpha_\nu}$) and peak flux density ($F_p(t) = F_{p,0}(t/T_0)^{-\alpha_F}$), where our reference epoch is $T_0 + 75$ days. We assume constant spectral indices $b_1 = b_2 = -1$ and a common $s = 1$. Fitting all of our radio data within this framework leaves five free parameters: $F_{p,0}$, α_F, $\nu_{b,0}$, α_ν, and b_1. As shown in Figure 3(b) this model is unable to satisfactorily fit the entire set of radio observations. The model underpredicts the peak flux at our best sampled epoch, while overpredicting the later-time data (especially at frequencies close to 10 GHz while being in marginal contention with lower-frequency data). This is not unprecedented for FBOTs. AT 2018cow also demonstrated a significant change in its radio evolution at $\approx$20 days, with the flux density dropping off markedly faster than predicted by an extrapolation of fits to the early-time data (Margutti et al. 2019). We were able to achieve better fitting results when using only the subset of our data at $\delta t \leqslant T_0 + 75$ days, with the results shown in Figure 3(c) and the best-fit model parameters given in Table 5. In the following discussion we adopt the model parameters derived for the fits to the subset of data taken at and before $\delta t \sim T_0 + 75$ days (Figure 3(c)) when inferring physical parameters. This allows us to better compare with our CXO observations (which were taken before 75 days), and to account for our best sampled radio SEDs. We will discuss possible interpretations of the late-time ($\delta t > T_0 + 75$ days) radio flux in Section 4.2.

3.3. Physical Parameters at $\delta t \lesssim T_0 + 75$ days

Using the results of our fitting in Section 3.2, we can infer physical parameters of the emitting region based on some simple assumptions. Following Chevalier & Fransson (2006), we calculate the forward shock radius R_p, the magnetic field B_p, the density of the CSM n, and the shock energy U_p, all as functions of time and accounting for the significant redshift of AT 2020xnd (which we describe in more detail in Appendix A). We further adopt fiducial values for the shock microphysical parameters of $\epsilon_e = 0.1$, $\epsilon_B = 0.01$, and an emitting volume fraction $f = 0.5$ (compared to a sphere of radius R_p). We let $\alpha \equiv f\epsilon_e/(0.5\epsilon_B)$, which encapsulates the main assumptions of our model.

The radius of the forward shock is

$$R_p = 4 \times 10^{14}\, \alpha^{-1/19}\left(\frac{F_p(1+z)^{-1}}{\rm mJy}\right)^{9/19}\left(\frac{D_\theta}{\rm Mpc}\right)^{18/19} \times \left(\frac{\nu_b(1+z)}{5\ {\rm GHz}}\right)^{-1} {\rm cm}, \quad (2a)$$

while its temporal evolution is modeled as

$$R_p = R_{p,0}\left(\frac{t}{T_0}\right)^{\alpha_\nu - (9/19)\alpha_F} = R_{p,0}\left(\frac{t}{T_0}\right)^{1.0\pm0.1}. \quad (2b)$$

Here $R_{p,0} = (2.8 \pm 0.2) \times 10^{16}$ cm is the value of R_p at our reference time (which we take to be $\delta t = T_0 + 75$ days post-explosion). We give statistical errors on the derived scalings, as well as the physical parameters, based on propagating the errors derived from our model fitting. We note, however, that systematic errors resulting from the model assumptions likely dominate. We can then infer the average velocity implied by

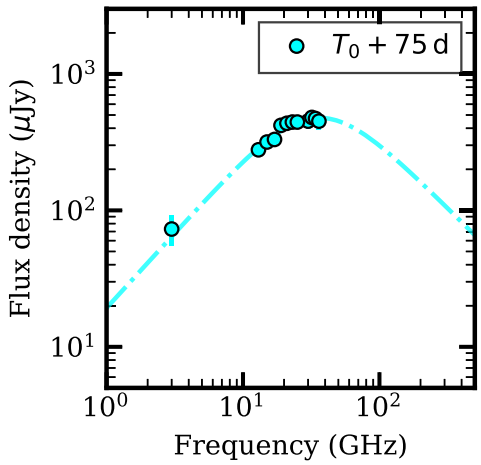

(a) Fitting data subset at $\delta t = T_0 + 75$ d.

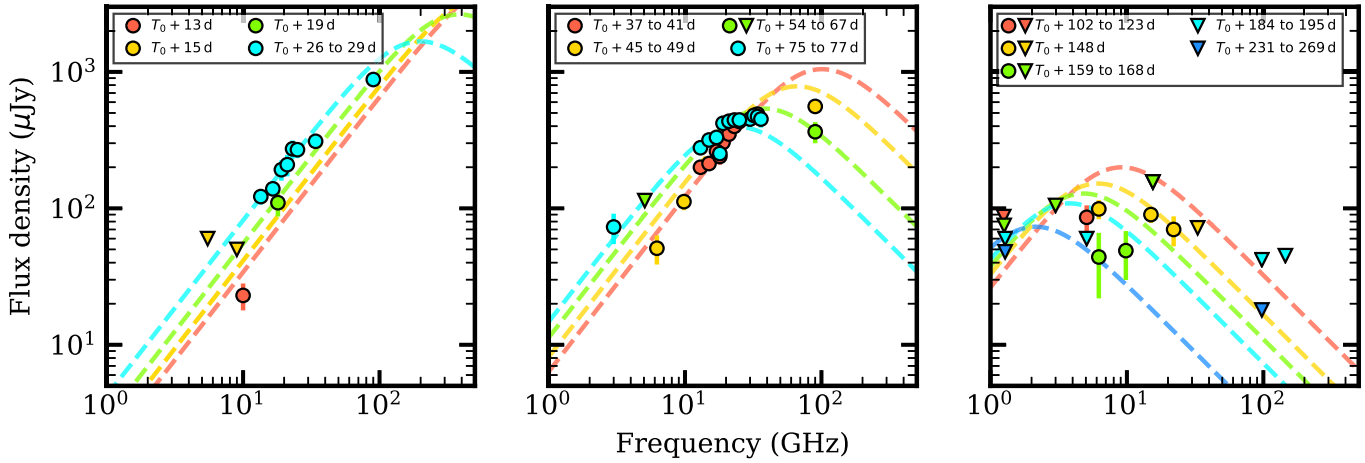

(b) Fitting all data.

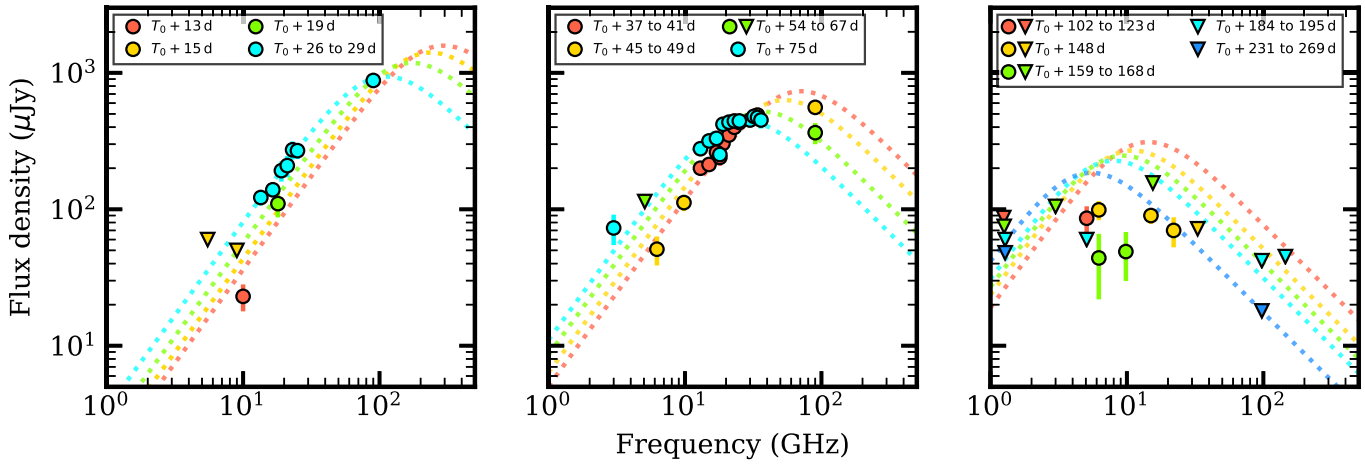

(c) Fitting data subset at $\delta t < T_0 + 75$ d.

Figure 3. Radio observations of AT 2020xnd taken with the VLA, ATCA, GMRT, GBT, MeerKAT, ALMA, AMI-LA, and eMERLIN radio telescopes, with best fits shown for the model described in Section 3.2. Curves are plotted at the mean time of the observations within the time ranges described in the legend. (a) Our best sampled radio SED, without considering any evolution of the break flux and frequency. (b) All radio observations of AT 2020xnd. The model fit describes the single-epoch data well. When considering the entire data set it is clear that the evolving SED model is in marginal contention with the late-time low-frequency data from MeerKAT at $\delta t > 191$ days, overpredicts data at $\delta t = T_0 + 148$ days and $\delta t = T_0 + 167$ days, but underpredicts the epoch at $\delta t = T_0 + 75$ days. (c) Radio observations at $\delta t \leqslant T_0 + 75$ days. The best-fit model parameters and the inferred physical parameters for the data subsets in (a), (b), and (c) are given in Table 5 and Table 6, respectively.

Table 5
Best-fit Parameters for Different Subsets of Our Radio Data, Fit with Equation (1)

Data Subset	$\log(\nu_{b,0}/\mathrm{GHz})$[a]	$\log(2^s F_{p,0}/\mu\mathrm{Jy})$[a]	b_1	b_2	α_F	α_ν	s	χ^2_ν
$t = t_0 + 75$ days	1.54 ± 0.09	3.28 ± 0.03	1.1 ± 0.2	-1	0	0	1	0.4
All	1.34 ± 0.02	3.20 ± 0.01	1.29 ± 0.06	-1	1.40 ± 0.08	2.03 ± 0.09	1	3.1
$t \leqslant t_0 + 75$ days	1.39 ± 0.03	3.24 ± 0.02	1.37 ± 0.07	-1	0.7 ± 0.1	1.3 ± 0.1	1	2.1

Note. Values given without errors are fixed when performing the fit.
[a] Quantities with a subscript 0 are defined at $T_0 + 75$ days.

Table 6
Physical Parameters as Measured at the Reference Time

Data Subset	$R_{p,0}$ ($\times 10^{16}$ cm)	$B_{p,0}$ (G)	$(\Gamma\beta c)_{p,0}$	$U_{p,0}$ ($\times 10^{50}$ erg)	$n_{p,0}$ ($\times 10^5$ cm^{-3})	$\dot{M}_{p,0}$ ($\times 10^{-3}\, M_\odot$ yr^{-1})	$\nu_{c,p,0}$ (GHz)
$t = t_0 + 75$ days	2.0 ± 0.4	1.5 ± 0.3	0.13 ± 0.03	1.5 ± 0.4			20 ± 10
All	2.9 ± 0.2	0.96 ± 0.05	0.19 ± 0.01	1.9 ± 0.1	1.0 ± 0.2	2.7 ± 0.5	70 ± 10
$t \leqslant t_0 + 75$ days	2.8 ± 0.2	1.04 ± 0.07	0.18 ± 0.01	2.0 ± 0.2	1.3 ± 0.2	3.2 ± 0.7	50 ± 10

Note. See main text for parameter scaling. Values assume $\epsilon_e = 0.1$, $\epsilon_B = 0.01$, and $f = 0.5$. For the mass-loss rate we assume a wind velocity of 1000 km s^{-1}. The errors reported here are the result of propagating the uncertainties in the fit parameters reported in Table 5; they are likely underestimated due to inherent uncertainties associated with the assumptions made in our model. Due to the large uncertainty in the radius for our model fit to the data taken at 75 days post-explosion, we do not give a density or mass loss.
[a] Quantities with a subscript 0 are defined at $T_0 + 75$ days.

our model as $(\beta\Gamma c)_p = R_p(1+z)/t_0$ (which is 0.18 ± 0.02 at 75 days post-explosion). The best-fit model to these data is consistent with no acceleration ($R_p \propto t^{1.0\pm0.1}$), although we only confidently measure the location of the peak at the reference epoch. As a comparison, fitting only the data at $\delta t = T_0 + 75$ days, we infer a shock radius of $(2.0 \pm 0.7) \times 10^{16}$ cm at this epoch, implying an average outflow velocity of the fastest ejecta of $\Gamma\beta c = R(1+z)/t = 0.13 \pm 0.04$. Note that the dependence on the shock microphysical parameters is minor, with an order-of-magnitude change in α resulting in a $\sim$10% change in the radius and velocity (see Equation (2a)).

The magnetic field and its scaling are given in Equations (3a) and (3b), respectively:

$$B_p = 1.1\alpha^{-4/19}\left(\frac{F_p(1+z)^{-1}}{\mathrm{mJy}}\right)^{-2/19}\left(\frac{D_\theta}{\mathrm{Mpc}}\right)^{-4/19} \times \left(\frac{\nu_b(1+z)}{5\ \mathrm{GHz}}\right)\mathrm{G} \quad (3a)$$

$$B_p = B_{p,0}\left(\frac{t}{T_0}\right)^{(2/19)\alpha_F - \alpha_\nu} = B_{p,0}\left(\frac{t}{T_0}\right)^{-1.3\pm0.1}. \quad (3b)$$

Here $B_{p,0}$ is the value of B_p, the magnetic field associated with the self-absorbed synchrotron emission, at our references time. Note again that, similar to the radius, the value of the magnetic field is relatively robust to the choice of α. We find $B_{p,0} = 1.04 \pm 0.07$ G. Fitting the SED at $\delta t = T_0 + 75$ days in isolation, we find a post-shock magnetic field of 1.5 ± 0.3 G. These values are similar to those of SNe and other FBOTs (e.g., Chevalier & Fransson 2006; Margutti et al. 2019; Ho et al. 2020b; Coppejans et al. 2020).

Additionally, the peak flux and break frequency allow us to constrain a density profile for the CSM, which was crafted by the mass-loss history of the progenitor star that the SN outflow is interacting with. The density profile of the CSM can be written as $\rho = \dot{M}/(4\pi r^2 v_w) = Ar^{-2}$, where $\dot{M}$ is the mass-loss rate of the star with wind of velocity v_w. We define $A_\star \equiv A/(5 \times 10^{11}\ \mathrm{g\ cm^{-1}})$ so that $A_\star = 1$ for $\dot{M} = 10^{-5}\, M_\odot$ yr^{-1} and $v_w = 1000$ km s^{-1}, which are typical of Wolf–Rayet stars. Under the assumption that a fraction ϵ_B of the shock energy density is converted to magnetic energy density, $A_\star$ can be defined as in Equation (4a) and the scaling resulting from our models as in Equation (4b):

$$A_{\star p} = \alpha^{-8/19}\left(\frac{\epsilon_B}{0.1}\right)^{-1}\left(\frac{F_p(1+z)^{-1}}{\mathrm{mJy}}\right)^{-4/19}\left(\frac{D_\theta}{\mathrm{Mpc}}\right)^{-8/19} \times \left(\frac{\nu_b(1+z)}{5\ \mathrm{GHz}}\right)^2\left(\frac{t(1+z)^{-1}}{10\ \mathrm{days}}\right)^2 \quad (4a)$$

$$A_{\star p} = A_{\star p,0}\left(\frac{t}{t_0}\right)^{(4/19)\alpha_F - 2\alpha_\nu + 2} = A_{\star p,0}\left(\frac{t}{t_0}\right)^{-0.5\pm0.2}. \quad (4b)$$

For the best-fit parameters of our model we find that $A_{\star p,0} = (90 \pm 10) \times \alpha^{-8/19}(\epsilon_B/0.1)^{-1}$ or $A = (1.8 \pm 0.2) \times 10^{13}$ g cm^{-1} for $\alpha = 10$. The dependence of $A_{\star,p}$ on the plasma microphysical parameters is more pronounced than for the radius and magnetic field. Using the scaling derived in Equation (2b), we see that, under the assumption that the CSM is dominated by fully ionized hydrogen, the number density profile is

$$n\left(\frac{R_p}{R_{p,0}}\right) = 5 \times 10^{11} m_p^{-1}\left(\frac{A_{\star p,0}}{R_{p,0}^2}\right)\left(\frac{R_p}{R_{p,0}}\right)^{\frac{22\alpha_F - 76\alpha_\nu + 38}{19\alpha_\nu - 9\alpha_F}}\ \mathrm{cm^{-3}}, \quad (5)$$

and therefore $n = n_{p,0}(R_p/R_{p,0})^{-2.5\pm0.2}$. From the previously calculated values of $A_{\star p,0}$ and $R_{p,0}$, we see that $n_{p,0} = (1.3 \pm 0.2) \times 10^4$ cm^{-3} at a radius of $R_p \sim 2.8 \times 10^{16}$ cm (i.e., $R_{p,0}$). These values imply effective mass-loss

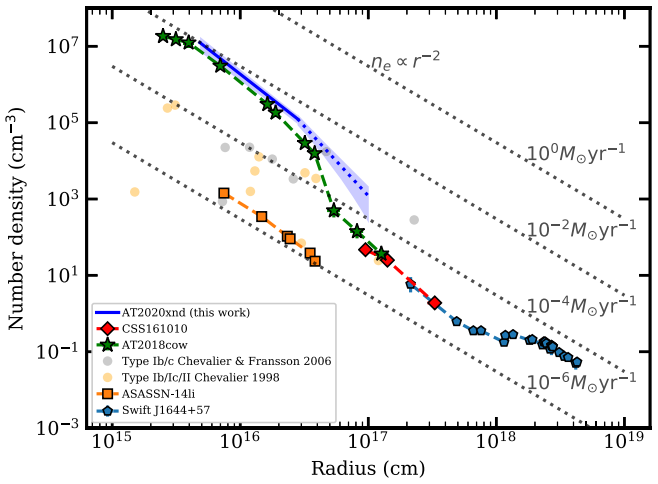

Figure 4. The particle number density as a function of radius for the FBOTs AT 2020xnd including the possible steepening at $\delta t \sim T_0 + 75$ days (this work), CSS 161010 (Coppejans et al. 2020), and AT 2018cow (Nayana & Chandra 2018; Ho et al. 2019b; Margutti et al. 2019). Also shown are single measurements from various Type Ib/c and Type II SNe where we derived the number density using values from Chevalier & Fransson (2006) and Chevalier (1998). Additionally, we include measurements of number density from the prototypical thermal and nonthermal TDEs, ASASSN-14li and Swift J1644 +57, respectively (Alexander et al. 2016; Eftekhari et al. 2018). Note that the densities derived for the two TDEs used the results of Barniol Duran et al. (2013) as opposed to Chevalier & Fransson (2006) in this work. Dotted gray lines show different rates of constant mass loss ($n_e \propto r^{-2}$ and assuming a wind velocity of 1000 km s^{-1}). FBOTs show preferentially high densities and therefore larger mass-loss rates than the Type-Ibc/Ic/II events presented in Chevalier (1998) and Chevalier & Fransson (2006).

rates $\dot{M} \sim 3 \times 10^{-3}\, M_\odot\ \mathrm{yr}^{-1}$ for $v_w = 1000\,\mathrm{km\ s}^{-1}$. We compare the density profile of AT 2020xnd with other classes of SNe and FBOTs in Figure 4. The inferred density of the environment of AT 2020xnd is very similar to that of the FBOT AT 2018cow, and denser than typical SN environments. While similarly large densities can be found around supermassive black holes, dormant intermediate-mass black holes (IMBHs) are not expected to be surrounded by high-density media. This provides challenges for FBOT models invoking a tidal disruption event (TDE) around an IMBH (e.g., Kuin et al. 2019; Perley et al. 2019). By the end of our observing campaign we are probing emission at $\sim 10^{17}$ cm. Taking our number density profile and integrating it out to this radius implies a total mass swept up of $\sim 10^{-2}\ M_\odot$.

Finally, we calculate the shock energy according to

$$U_p = \left(\frac{fR^3B^2}{6\epsilon_B}\right) = 1.3 \times 10^{43} f \epsilon_B^{-1} \alpha^{-11/19} \left(\frac{F_p(1+z)^{-1}}{\mathrm{mJy}}\right)^{23/19} \times \left(\frac{D_\theta}{\mathrm{Mpc}}\right)^{46/19} \left(\frac{\nu_p(1+z)}{5\ \mathrm{GHz}}\right)^{-1} \mathrm{erg} \quad (6a)$$

$$U_p = U_{p,0}\left(\frac{t}{t_0}\right)^{\alpha_\nu - (23/19)\alpha_F} = U_{p,0}\left(\frac{t}{t_0}\right)^{0.5\pm0.3} \quad (6b)$$

and find that, $U_p = (1.5 \pm 0.1) \times 10^{49} f \epsilon_B^{-1} \alpha^{-11/19}$ erg or $U_p = (2.0 \pm 0.2) \times 10^{50}$ erg, for our fiducial f, α, and ϵ_B parameters. U_p has a similar dependence on the plasma microphysical parameters to $A_{\star,p}$. For comparison, the single SED fit at 75 days returned a total shock energy of $U = (1.5 \pm 0.4) \times 10^{50}$ erg. For comparisons, AT 2018cow showed significantly less energy ($U \sim 5 \times 10^{47}$ erg) at similar epochs (Margutti et al. 2019, D. Coppejans et al., in preparation), while the mildly relativistic FBOT CSS 161010 was powered by a similarly energetic outflow with $U = (2.9 \pm 0.1) \times 10^{49}$ erg (Coppejans et al. 2020).

3.4. Late-time Emission at $\delta t > 75$ days: Submillimeter and Low-frequency Constraints

As discussed in the previous sections, a single power-law evolution of the peak flux and peak frequency with time is unable to provide an accurate representation of the entire data set. Our data coverage is sparser at $\delta t > T_0 + 75$ days, but the data indicate a significantly faster evolution. In this time range we find $\alpha_\nu = 2.1 \pm 0.4$ and $\alpha_F = 2.2 \pm 0.2$, which we calculate by fitting just the SEDs at $\delta t = T_0 + 75$ days and $\delta t = T_0 + 148$ days. Interestingly, these imply a steepening of the density profile as $n \propto (R/R_0)^{3.6\pm0.6}$ around $R_p \sim 3 \times 10^{16}$ cm. A similar steepening was inferred for the environment of AT 2018cow and might represent a defining characteristic of the class of luminous FBOTs. We will discuss possible origins of this density profile in Section 4.2.

3.5. Synchrotron Cooling

The frequency of the cooling break (where the electrons are radiating a significant fraction of their energy to synchrotron radiation on a dynamical timescale) can be estimated as $\nu_c = (18\pi m_e c e)/(t^2 \sigma_t^2 B^3)$ where we can use our estimates for the magnetic field made in the previous section. For our best-fit model parameters (for data taken at $\delta t \leqslant T_0 + 75$ days) we see that $\nu_c = \nu_{c,0}(t/t_0)^{1.6\pm0.4}$ GHz, with $\nu_{c,0} = 70 \pm 10$ GHz (we stress, however, that these calculations are only strictly valid for a constant magnetic field and depend quite strongly on α). At the same time the synchrotron frequency is $\nu_m \equiv \gamma_m^2 (eB/2\pi m_e c) \approx 3\gamma_m^2$ MHz, so we have that $\nu_m < \nu_{\rm sa} < \nu_c$ for $\gamma_m \lesssim 170$. The synchrotron spectrum from a population of electrons accelerated into a power-law distribution with an index p governing their energy distribution steepens from $F_\nu \propto \nu^{-(p-1)/2}$ to $F_\nu \propto \nu^{-p/2}$ above the cooling break (in the event that $\nu_{\rm sa} < \nu_m < \nu_c$ or $\nu_m < \nu_{\rm sa} < \nu_c$; see, e.g., Granot & Sari 2002).

We show the cooling break in the context of the radio through X-ray SED in Figure 5 for data taken at our reference epoch, along with the two epochs with quasi-simultaneous CXO and radio observations. At early times $\nu_c < \nu_{\rm sa}$ (which might be contributing to "broadening" the synchrotron cooling break) and the optically thin spectrum never demonstrates the $F_\nu \propto \nu^{-(p-1)/2}$ scaling, instead moving directly to the $F_\nu \propto \nu^{-p/2}$ regime. Accounting for the presence of synchrotron cooling demonstrates that the X-rays are in a significant excess to the radio data taken at approximately the same time, as found for the other FBOTs with both radio and X-ray data, CSS 161010 and AT 2018cow (Margutti et al. 2019; Coppejans et al. 2020). The presence of a luminous X-ray excess of emission appears to be a defining property of optically luminous FBOTs (further discussed in Section 4.1).

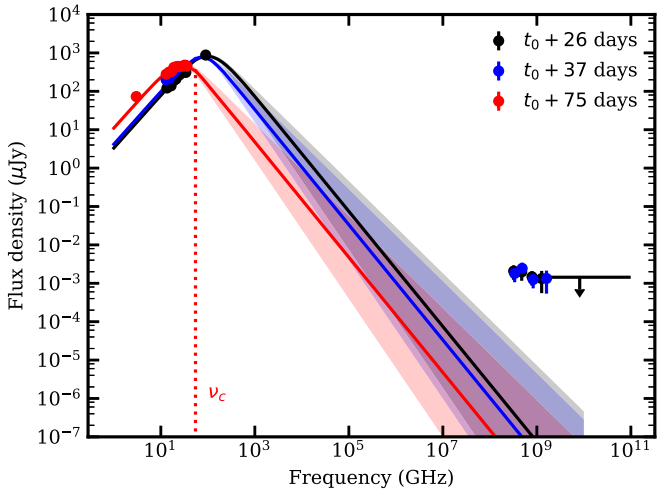

Figure 5. The radio through X-ray SED of AT 2020xnd showing our two Chandra epochs and the two nearest-in-time VLA epochs. Also shown is the reference epoch where we best sample the peak of the radio SED. Under the assumption that the peak of the SED is the result of synchrotron self-absorption we estimate the location of the synchrotron cooling break, ν_c, at the reference epoch, and demonstrate this here. Due to the magnetic field scaling derived in Section 3.5 the cooling break should move to higher frequencies with time. At the black and blue epochs we are in the regime where ν_m, $\nu_c < \nu_{sa}$, and the cooling break is not seen. Instead we show these epochs with the slope at frequencies higher than the self-absorption frequency steepened from $-(p-1)/2$ to $-p/2$. The wide upper limit given at epoch 1 is from NuSTAR and includes the entire 3–79 keV observing band. Constraints at the other epochs were comparable. While we fix the post-break spectral index to be -1 in our model, the shaded regions show the effect of including an error of ± 0.3 on this value.

4. Discussion

4.1. An X-Ray Excess

We detected AT 2020xnd on three epochs with the Chandra X-ray Observatory, with a significant drop occurring between our second and third observations (see Figure 2). We show the radio through X-ray SED of AT 2020xnd in Figure 5, demonstrating the location of the cooling break at various epochs. It is clear that, as for the other two FBOTs with both X-ray and radio detections, the extrapolated radio spectrum predicts less X-ray emission than observed. This is the case even considering a relatively large error on the post-break spectral index. From our Chandra observations of AT 2020xnd we can measure the photon index to be $\Gamma = \beta + 1 = 1.4^{+0.33}_{-0.33}$. This is a shallower (harder) spectrum than we would expect for the fast cooling regime in the X-rays ($\Gamma = 2$ to 2.5), further suggesting a different origin for the X-ray emission in addition to (and consistent with) our assessment based on the X-ray flux level. Similar considerations based on similar observational evidence led Margutti et al. (2019) to suggest the presence of a centrally located source of hard X-ray emission in AT 2018cow.

In stark contrast to normal SNe (see, e.g., SN 2014C; Margutti et al. 2017), the X-ray emission in AT 2018cow is of clear *nonthermal* origin (Margutti et al. 2019). An intriguing possibility is that the source of energy of AT 2018cow might be connected to energy released by a newly formed compact object, in the form of either a black hole or a neutron star. With $L_X \approx 6 \times 10^{42}$ erg s^{-1} (Figure 2), the measured X-ray luminosity of AT 2020xnd is ≈5 orders of magnitude larger than the Eddington luminosity for a stellar mass black hole (see Table 3). This is similar to what was seen in the FBOTs AT 2018cow and CSS 161010 (Margutti et al. 2019; Coppejans et al. 2020), confirming that FBOTs with associated X-ray emission have a similar luminosity to TDEs and GRBs in the local universe, and are significantly more luminous than "normal" CCSNe (see, e.g., Margutti et al. 2013a, 2013b, 2017; Drout et al. 2014; Vinkó et al. 2015; Eftekhari et al. 2018 for luminosities of these various transient classes).

If the X-ray emission from FBOTs is powered by a nebula of relativistic particles energized by a central engine, the sudden drop in the X-ray luminosity could in principle arise from an abrupt shift in the spectral energy distribution of the emission rather than change in the bolometric decay of the engine's luminosity (which is generally predicted to be smooth in fallback accretion or magnetar-powered scenarios). For example, in their recent self-consistent Monte Carlo calculations of jet/magnetar-powered nebulae and engine-powered transients, Vurm & Metzger (2021) predict that, for FBOT-scaled engine and ejecta properties, an abrupt increase in the mean energy per particle is predicted to occur on a timescale of ∼1 month after the explosion due to a change in the processes regulating the mass-loading of the wind/jet (namely, the cessation of $\gamma\gamma$ pair production). The resulting sudden increase in the peak of the nonthermal synchrotron or inverse Compton emission could act to shift the radiated energy from the soft X-ray to the gamma-ray band (where it would go undetected at these relatively late epochs).

4.2. Late-time Radio Emission

Interestingly, as with the other radio-loud FBOTs with well monitored radio emission, we were not able to describe the entire data set of AT 2020xnd with an evolving broken power law as given by Equation (1) (Margutti et al. 2019; Coppejans et al. 2020; D. Coppejans et al., in preparation). This is the result of a sharp late-time drop-off in radio flux that we speculate is a defining characteristic of FBOTs. In normal SNe, F_p tends to remain constant in time, while $\nu_p \propto t^{-1}$, which leads to the characteristic $F_\nu \propto t^{-1}$ in the optically thin regime that is appropriate at these late epochs. The markedly different rate of decay of the radio flux density of FBOTs versus normal SNe after peak can be immediately appreciated from Figure 2. From a physical perspective, this fast evolution can be the result of a steeply decaying density of the environment at larger radii, moving from $\rho \propto (R/R_0)^{2.5\pm0.2}$ at $\delta t \lesssim T_0 + 75$ days to $\rho \propto (R/R_0)^{3.6\pm0.6}$ afterwards (determined by fitting the evolution between the SEDs at $\delta t = T_0 + 75$ days and $\delta t = T_0 + 148$ days (see Figure 4). This is inferred from the peak flux density decaying faster at later times ($\alpha_F = 0.7 \pm 0.1$ to $\alpha_F = 2.2 \pm 0.2$), and the break frequency moving faster to lower frequencies ($\alpha_\nu = 1.3 \pm 0.1$ to $\alpha_\nu = 2.1 \pm 0.4$). However, we emphasize that in the context of our synchrotron formalism where the shock microphysics parameters are constant with time, an equivalent interpretation of the steeply decaying $F_p(t)$ and $\nu_p(t)$ parameters would be that of a rapidly evolving $B(R)$. The fast evolution could also be the result of a decelerating blast wave; however, the large errors when jointly fitting the $\delta t = T_0 + 75$ days and $\delta t = T_0 + 148$ days SEDs prevent us from determining the evolution of the radius between these epochs.

4.3. Free–Free Absorption

Due to the high densities of the environment we derive based on our radio SED modeling, we consider the potential effects of free–free absorption on the observed radio SED, which would manifest as a sharp drop-off at low frequencies (and hence an optically thick flux density $F_\nu \propto \nu^\beta$ with $\beta > 5/2$; e.g., Weiler et al. 2002). Our SEDs do not show any evidence for free–free absorption. Following Margutti et al. (2019), we have that the optical depth to free–free absorption is

$$\tau_{\rm ff} \approx \frac{\alpha_{\rm ff} r}{3} \approx 10\left(\frac{\nu}{10\ {\rm GHz}}\right)^{-2}\left(\frac{T_g}{10^4\ {\rm K}}\right)^{-3/2}\left(\frac{A}{100A_\star}\right)^2 \times \left(\frac{v}{0.1c}\right)^{-3}\left(\frac{t}{\rm week}\right)^{-3}. \quad (7)$$

Here $\alpha_{\rm ff}$ is the absorption coefficient of free–free absorption, T_g is the temperature of the absorbing gas, and v is the shock velocity. The subset of our data at $t \lesssim T_0 + 76$ days shows a spectral index broadly consistent with synchrotron self-absorbed emission (although with a shallower self-absorption index than the expected $F_\nu \propto \nu^2$ for $\nu_m < \nu < \nu_{\rm sa}$). Free–free absorption will become prevalent when $\tau_{\rm ff} \gtrsim 1$, so the lack of any obvious spectral drop-off at low frequencies at any of our epochs implies that $\nu_{{\rm ff},\tau=1} \ll \nu_p$. Using the epoch at $t = T_0 + 75$ days, this implies $\nu_{{\rm ff},\tau=1} \ll 40$ GHz.

We can then use this observational constraint and Equation (7) to place a constraint on the density of the environment as

$$\frac{A}{A_\star} \lesssim 300\left(\frac{T_g}{10^4}\right)^{3/4} v_{0.1}^{3/2} \quad (8)$$

at $t = T_0 + 75$ days. This is consistent with the values derived in Section 3.3 for our derived outflow velocities.

4.4. Rapid X-Ray Decline

We show our Chandra X-ray observations of AT 2020xnd in Figure 2 along with those from CSS 161010 and the well sampled AT 2018cow. A striking feature of the X-ray emission is the significant increase in the rate of flux decay seen at ∼20 days post-discovery (in the target's rest frame). AT 2018cow initially declined according to $F_{\rm X} \propto t^{-1}$ before a steepening occurred, changing the decay rate to $F_{\rm X} \propto t^{-4.5}$. The optical properties of AT 2018cow appeared to morph on a similar epoch, with the previously featureless optical spectrum showing H and He emission lines with a corresponding velocity of ∼4000 km s^{-1}, and a high photospheric temperature that showed little evolution (Perley et al. 2021). Based on the optical data presented by Perley et al. (2021), AT 2020xnd appears to show similar properties, although a lack of optical spectra taken around 20 days post-discovery prevents us from confirming the link between X-ray and optical evolution.

The X-ray fading seen in AT 2018cow was in no way smooth, with a high level of variability seen on timescales of less than a day (Margutti et al. 2019); however, due to the relative faintness of AT 2020xnd we could not perform a similar analysis in this work. Sudden changes in the X-ray properties of engine-powered transients/variables are commonly seen in X-ray binary (XRB) systems as sources transition between accretion states (Fender et al. 2004; Remillard & McClintock 2006). XRBs, however, have X-ray luminosities (attributed to accretion) at approximately, or considerably less than, the Eddington limit, with changes in the X-ray hardness/luminosity (as well as their radio properties; see, e.g., Bright et al. 2020b) seen at ∼1% $L_{\rm Edd}$. Due to the extremely high X-ray luminosity of the FBOTs (e.g., many orders of magnitude above the Eddington limit for AT 2020xnd), attributing the evolving X-ray evolution of AT 2018cow/AT 2020xnd to a similar mechanism is challenging because accretion rates this large are simply not seen in Galactic transients, with only the ultraluminous X-ray sources exceeding the Eddington limit.

5. Conclusions

AT 2020xnd is now the fourth FBOT to be detected at radio frequencies, and the third at X-rays. Our analysis of the evolving radio and X-ray emission allows us to draw a number of key conclusions on the nature of this object.

1. The fastest outflows produced by AT 2020xnd (probed through our radio observations) traveled at a significant fraction of the speed of light ($0.1c$–$0.2c$), a result that is robust to the subset of data that we fit, and also only weakly depends on the model assumptions. Our derived outflow velocity, and the energy contained within the outflow, are compared to those from SNe and GRBs in Figure 6.
2. Our observations strengthen the case for FBOTs hosting a central engine. Our X-ray observations are both spectrally harder than, and in excess of, extrapolations of our fits to the radio data. This implies a distinct emission component producing X-rays in AT 2020xnd. Despite observing AT 2020xnd in hard X-rays with NuSTAR we were unable to place meaningful constraints on any hard X-ray excess, as seen in AT 2018cow.
3. Similar to AT 2018cow, the X-ray emission from AT 2020xnd underwent a marked change in its decay rate at ∼20 days post=explosion. While the physical cause of this evolution remains unclear, it motivates further X-ray studies of FBOTs.
4. We see a distinct change ($\alpha_F = 0.7 \pm 0.1$ to $\alpha_F = 2.2 \pm 0.2$; $\alpha_\nu = 1.3 \pm 0.1$ to $\alpha_\nu = 2.1 \pm 0.4$) in the late-time evolution of the radio SED from AT 2020xnd, revealed through our inability to find a satisfactory fit to the entirety of our radio observations with a single evolving synchrotron spectrum. Our attempts led to a model underpredicting our most well sampled radio epoch, and moderately overpredicting the late-time data at low frequencies. A similar phenomena was seen (and more clearly) in AT 2018cow (D. Coppejans et al., in preparation).
5. We find broad agreement with the results obtained by Ho et al. (2021b) for their independent analysis of a separate data set from AT 2020xnd. This includes a similar shock velocity, energy, and steep density profile, with a change in shock properties occurring at around $\delta t = T_0 + 75$ days. This change in parameters also prevented them from fitting a single evolving synchrotron self-absorbed SED. Furthermore, they also find X-ray emission in excess of an extrapolation of the radio emission, thus requiring a separate emission component. The physical parameters derived in Ho et al. (2021b) are the result of

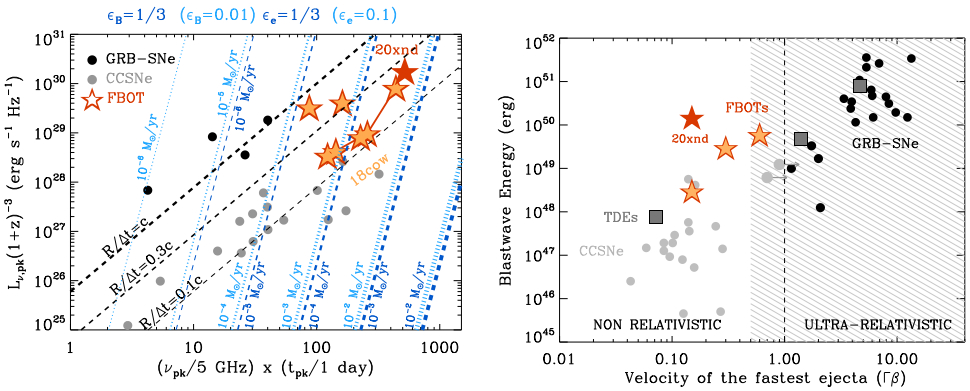

Figure 6. Left: radio phase space of stellar explosions, where $L_{\nu,\rm pk}$ is the spectral peak luminosity, $\nu_{\rm pk}$ is the spectral peak frequency, and $t_{\rm pk}$ is the peak time. Normal core-collapse stellar explosions (CCSNe, gray filled circles) typically show a shock velocity $\sim 0.1c$, while GRB–SNe (black filled circles) are characterized by significantly faster shocks. The new class of multiwavelength FBOTs (stars) currently comprises four elements and shows a variety of shock velocities that bridge the gap between normal SNe (e.g., AT 2018cow) and the ultrarelativistic jets of GRBs (e.g., CSS 161010, AT 2018lug, and AT 2020nxd). The dashed dark (dotted light) blue lines are lines of constant equivalent mass-loss rate for an assumed wind velocity $v_w = 1000$ km s^{-1} for equipartition parameters $\epsilon_B = \epsilon_e = 1/3$ ($\epsilon_B = 0.01$, $\epsilon_e = 0.1$). Black dashed lines: lines of constant apparent velocity $R/\Delta t$ under the assumption of equipartition. The factor $(1+z)^{-3}$ accounts for the difference between the angular distance and the luminosity distance. Right: shock energy versus fastest ejecta velocity for a variety of transients, including TDEs, SNe, and FBOTs. FBOTs represent a new class of transients with energetic shocks that can be transrelativistic. Among FBOTs, AT 2020xnd shows the largest equipartition energy. The color coding is the same as in the left panel. The shaded region shows the parameter space of engine-driven explosions. References: Margutti et al. (2019); Ho et al. (2019b); Coppejans et al. (2020).

the same synchrotron self-absorption modeling discussed in this work; however, Ho et al. (2021b) assume equipartition with $\epsilon_B = \epsilon_e = 1/3$. This difference (coupled with different measurements of the peak flux density and peak frequency) leads us to derive a $\sim$2 times larger magnetic field, but with consistent radii. The main different is in the shock energy, which scales as $(\epsilon_e/\epsilon_B)^{-11/19}\epsilon_B^{-1}$, leading to an order-of-magnitude difference in the energy estimate. The choice of microphysical parameters can have a similarly large effect on the estimate for the CSM density and inferred mass-loss rate.

These properties continue to confirm FBOTs as a new and distinct class of extragalactic transient with luminous counterparts outside the optical spectrum. As surveys such as ZTF and The Young Supernova Experiment (YSE) continue to probe events evolving on short timescales, only through extensive multiwavelength follow-up will the intrinsic nature of fast blue optical transients be revealed.

We thank the anonymous referee for their comments that helped improve this manuscript. We thank Anna Ho for sharing an advanced copy of her manuscript with us. Raffaella Margutti's team at Berkeley and Northwestern is partially funded by the Heising-Simons Foundation under grant # 2018-0911 (PI: Margutti). Support for this work was provided by the National Aeronautics and Space Administration through Chandra Award Number GO1-22062X issued by the Chandra X-ray Center, which is operated by the Smithsonian Astrophysical Observatory for and on behalf of the National Aeronautics and Space Administration under contract NAS8-03060. R.M. acknowledges support by the National Science Foundation under Award No. AST-1909796 and AST-1944985. R.M. is a CIFAR Azrieli Global Scholar in the Gravity & the Extreme Universe Program, 2019 and an Alfred P. Sloan fellow in Physics, 2019. W.J-G. is supported by the National Science Foundation Graduate Research Fellowship Program under Grant No. DGE-1842165 and the IDEAS Fellowship Program at Northwestern University. W.J-G acknowledges support through NASA grants in support of Hubble Space Telescope programs GO-16075 and GO-16500. The Berger Time-Domain Group at Harvard is supported in part by NSF and NASA grants. D.M. acknowledges NSF support from grants PHY-1914448 and AST-2037297.

This project makes use of the NuSTARDAS software package. We thank Rob Beswick and the eMERLIN team for approving and carrying out DDT observations of AT 2020xnd. We thank Jamie Stevens and the ATCA team for approving DDT observations of AT 2020xnd. The Australia Telescope Compact Array is part of the Australia Telescope National Facility which is funded by the Australian Government for operation as a National Facility managed by CSIRO. We acknowledge the Gomeroi people as the traditional owners of the Observatory site. The National Radio Astronomy Observatory is a facility of the National Science Foundation operated under cooperative agreement by Associated Universities, Inc. This paper makes use of the following ALMA data: ADS/JAO.ALMA#2019.1.01157.T. ALMA is a partnership of ESO (representing its member states), NSF (USA) and NINS (Japan), together with NRC (Canada), MOST and ASIAA (Taiwan), and KASI (Republic of Korea), in cooperation with the Republic of Chile. The Joint ALMA Observatory is operated by ESO, AUI/NRAO and NAOJ. The Green Bank Observatory is a facility of the National Science Foundation operated under cooperative agreement by Associated Universities, Inc. GMRT is run by the National Centre for Radio Astrophysics of the Tata Institute of Fundamental Research. The scientific results reported in this article are based in part on observations made by the Chandra X-ray Observatory. This research has made use of software provided by the Chandra X-ray Center (CXC) in the application packages CIAO. The MeerKAT telescope is operated by the South African Radio Astronomy Observatory, which is a facility of the National Research Foundation, an agency of the Department of Science and Innovation. Funding for SDSS-III has been provided by the Alfred P. Sloan Foundation, the Participating Institutions, the National Science Foundation, and the U.S. Department of

Energy Office of Science. The SDSS-III website is http://www.sdss3.org/. SDSS-III is managed by the Astrophysical Research Consortium for the Participating Institutions of the SDSS-III Collaboration including the University of Arizona, the Brazilian Participation Group, Brookhaven National Laboratory, Carnegie Mellon University, University of Florida, the French Participation Group, the German Participation Group, Harvard University, the Instituto de Astrofisica de Canarias, the Michigan State/Notre Dame/JINA Participation Group, Johns Hopkins University, Lawrence Berkeley National Laboratory, Max Planck Institute for Astrophysics, Max Planck Institute for Extraterrestrial Physics, New Mexico State University, New York University, Ohio State University, Pennsylvania State University, University of Portsmouth, Princeton University, the Spanish Participation Group, University of Tokyo, University of Utah, Vanderbilt University, University of Virginia, University of Washington, and Yale University. We thank the staff of the GMRT that made these observations possible. GMRT is run by the National Centre for Radio Astrophysics of the Tata Institute of Fundamental Research.

Facilities: ALMA, AMI-LA, ATCA, Chandra, eMERLIN, GBT, GMRT, MeerKAT, NuSTAR, Swift, VLA

Software: astropy, CASA (McMullin et al. 2007), MIRIAD (Sault et al. 1995), DDFacet (Tasse et al. 2018), killMS, matplotlib, numpy, oxkat (Heywood 2020), pandas (McKinney 2010), WSClean (Offringa et al. 2014; Offringa & Smirnov 2017).

Appendix A
Cosmological Modification to Chevalier (1998)

FBOTs occupy a unique region of the distance/outflow-velocity parameter space for radio transients. The inferred velocities are distinctly non-/mildly relativistic, significantly less than those associated with the distant GRBs (Barniol Duran et al. 2013) or Galactic X-ray binaries (Fender & Bright 2019) while having redshifts more comparable to the former and so must be accounted for. The measured flux density (specific flux) in the observer's frame (non-primed) is related to the specific luminosity in the source's rest frame (primed) by $F_\nu(\nu) = (1+z)L_\nu(\nu')/(4\pi D_L^2)$ (this is known as a K correction; see, e.g., Meyer et al. 2017; Condon & Matthews 2018) where D_L is the luminosity distance and $D_\theta = D_L(1+z)^{-2}$ is the angular diameter distance. We therefore have that $F_\nu(\nu) = (1+z)^{-3}L_\nu(\nu')/(4\pi D_\theta^2)$, where $\nu' = \nu(1+z)$ accounts for cosmological redshift. In Chevalier (1998) the angular extent of the source is given by $\theta = R/D$, which is the definition of the angular diameter distance. We wish to apply cosmological corrections to the observed quantities we use to make physical inferences on the forward-shock properties, which are the frequency of the spectral break, the time since explosion, and the flux density at the spectral break. The frequency and time are simple, and are given as $\nu' = \nu(1+z)$ and $t' = t(1+z)^{-1}$ (and therefore $\nu t = \nu' t'$ is independent of redshift). For the flux density we begin with our earlier definition $F_\nu(\nu) = (1+z)L_\nu(\nu')/(4\pi D_L^2)$, i.e., the flux density we measure corresponds to the luminosity at the redshifted frequency ν' with the factor $(1+z)$ accounting for the compressed bandwidth over which the flux density is measured in the observer's frame. The quantity $F'_\nu(\nu') = L_\nu(\nu')/(4\pi D_L^2)$ is the flux density of interest for the models of Chevalier (1998), being the flux density measured in the source frame at frequency ν'. We therefore have that $F'_\nu(\nu') = F_\nu(\nu)(1+z)^{-1}$ where the quantities on the right-hand side of the equality are all measurable. Throughout this work we give quantities in the non-primed (observer) frame and provide the appropriate redshift corrections in each formula for clarity.

ORCID iDs

Joe S. Bright https://orcid.org/0000-0002-7735-5796
Raffaella Margutti https://orcid.org/0000-0003-4768-7586
Deanne Coppejans https://orcid.org/0000-0001-5126-6237
Mark H. Wieringa https://orcid.org/0000-0002-7721-8660
Brian D. Metzger https://orcid.org/0000-0002-4670-7509
Lindsay DeMarchi https://orcid.org/0000-0003-4587-2366
Tanmoy Laskar https://orcid.org/0000-0003-1792-2338
Charles Romero https://orcid.org/0000-0001-5725-0359
Kate D. Alexander https://orcid.org/0000-0002-8297-2473
Assaf Horesh https://orcid.org/0000-0002-5936-1156
Giulia Migliori https://orcid.org/0000-0003-0216-8053
Ryan Chornock https://orcid.org/0000-0002-7706-5668
E. Berger https://orcid.org/0000-0002-9392-9681
Michael Bietenholz https://orcid.org/0000-0002-0592-4152
Mark J. Devlin https://orcid.org/0000-0002-3169-9761
Simon R. Dicker https://orcid.org/0000-0002-1940-4289
W. V. Jacobson-Galán https://orcid.org/0000-0002-3934-2644
Brian S. Mason https://orcid.org/0000-0002-8472-836X
Dan Milisavljevic https://orcid.org/0000-0002-0763-3885
Sara E. Motta https://orcid.org/0000-0002-6154-5843
Tony Mroczkowski https://orcid.org/0000-0003-3816-5372
Enrico Ramirez-Ruiz https://orcid.org/0000-0003-2558-3102
Craig L. Sarazin https://orcid.org/0000-0003-0167-0981
Jonathan Sievers https://orcid.org/0000-0001-6903-5074

References

Alexander, K. D., Berger, E., Guillochon, J., Zauderer, B. A., & Williams, P. K. G. 2016, ApJ, 819, L25
Alexander, K. D., van Velzen, S., Horesh, A., & Zauderer, B. A. 2020, SSRv, 216, 81
Arcavi, I., Wolf, W. M., Howell, D. A., et al. 2016, ApJ, 819, 35
Arnaud, K. A. 1996, in ASP Conf. Ser. 101, Astronomical Data Analysis Software and Systems V, ed. G. H. Jacoby & J. Barnes (San Francisco, CA: ASP), 17
Barniol Duran, R., Nakar, E., & Piran, T. 2013, ApJ, 772, 78
Bellm, E. C., Kulkarni, S. R., Graham, M. J., et al. 2019, PASP, 131, 018002
Bennett, C. L., Larson, D., Weiland, J. L., & Hinshaw, G. 2014, ApJ, 794, 135
Bright, J., Wieringa, M., Laskar, T., et al. 2020a, ATel, 14148, 1
Bright, J. S., Fender, R. P., Motta, S. E., et al. 2020b, NatAs, 4, 697
Bright, J. S., Horesh, A., van der Horst, A. J., et al. 2019, MNRAS, 486, 2721
Chevalier, R. A. 1998, ApJ, 499, 810
Chevalier, R. A., & Fransson, C. 2006, ApJ, 651, 381
Condon, J. J., & Matthews, A. M. 2018, PASP, 130, 073001
Coppejans, D. L., Margutti, R., Terreran, G., et al. 2020, ApJL, 895, L23
Dicker, S. R., Ade, P. A. R., Aguirre, J., et al. 2014, JLTP, 176, 808
Dobie, D., Ho, A., Perley, D. A., et al. 2020a, ATel, 14242, 1
Dobie, D., O'Brien, A., Ho, A., et al. 2020b, ATel, 14139, 1
Dobie, D., O'Brien, A., Ho, A., et al. 2020c, ATel, 14163, 1
Drout, M. R., Chornock, R., Soderberg, A. M., et al. 2014, ApJ, 794, 23
Eftekhari, T., Berger, E., Zauderer, B. A., Margutti, R., & Alexander, K. D. 2018, ApJ, 854, 86
Fender, R., & Bright, J. 2019, MNRAS, 489, 4836
Fender, R. P., Belloni, T. M., & Gallo, E. 2004, MNRAS, 355, 1105
Fong, W., Blanchard, P. K., Alexander, K. D., et al. 2019, ApJL, 883, L1
Fruscione, A., McDowell, J. C., Allen, G. E., et al. 2006, Proc. SPIE, 6270, 62701V
Graham, M. J., Kulkarni, S. R., Bellm, E. C., et al. 2019, PASP, 131, 078001
Granot, J., & Sari, R. 2002, ApJ, 568, 820
Heywood, I. 2020, oxkat: Semi-automated Imaging of MeerKAT Observations, Astrophysics Source Code Library, ascl:2009.003

Hickish, J., Razavi-Ghods, N., Perrott, Y. C., et al. 2018, MNRAS, 475, 5677
Ho, A. Y. Q., Margalit, B., Bremer, M., et al. 2021b, arXiv:2110.05490
Ho, A. Y. Q., Perley, D. A., Gal-Yam, A., et al. 2021a, arXiv:2105.08811
Ho, A. Y. Q., Perley, D. A., Kulkarni, S. R., et al. 2020b, ApJ, 895, 49
Ho, A. Y. Q., Perley, D. A., Kulkarni, S. R., et al. 2020c, ApJ, 895, 49
Ho, A. Y. Q., Perley, D. A., & Yao, Y. 2020a, TNSAN, 204, 1
Ho, A. Y. Q., Phinney, E. S., Ravi, V., et al. 2019a, ApJ, 871, 73
Ho, A. Y. Q., Phinney, E. S., Ravi, V., et al. 2019b, ApJ, 871, 73
Kalberla, P. M. W., Burton, W. B., Hartmann, D., et al. 2005, A&A, 440, 775
Kasliwal, M. M., Kulkarni, S. R., Gal-Yam, A., et al. 2010, ApJL, 723, L98
Kenyon, J. S., Smirnov, O. M., Grobler, T. L., & Perkins, S. J. 2018, MNRAS, 478, 2399
Kuin, N. P. M., Wu, K., Oates, S., et al. 2019, MNRAS, 487, 2505
Kurtzer, G. M., Sochat, V., & Bauer, M. W. 2017, PLoSO, 12, e0177459
Li, W., Chornock, R., Leaman, J., et al. 2011, MNRAS, 412, 1473
Margutti, R., Kamble, A., Milisavljevic, D., et al. 2017, ApJ, 835, 140
Margutti, R., Metzger, B. D., Chornock, R., et al. 2019, ApJ, 872, 18
Margutti, R., Soderberg, A. M., Wieringa, M. H., et al. 2013b, ApJ, 778, 18
Margutti, R., Zaninoni, E., Bernardini, M. G., et al. 2013a, MNRAS, 428, 729
Matthews, D., Margutti, R., Brethauer, D., et al. 2020, ATel, 14154, 1
McKinney, W, 2010, in Proc. of the 9th Python in Science Conf., ed. S. van der Walt & J. Millman (Austin, TX: SciPy), 56
McMullin, J. P., Waters, B., Schiebel, D., Young, W., & Golap, K. 2007, in ASP Conf. Ser. 376, Astronomical Data Analysis Software and Systems XVI, ed. R. A. Shaw, F. Hill, & D. J. Bell (San Francisco, CA: ASP), 127
Meyer, M., Robotham, A., Obreschkow, D., et al. 2017, PASA, 34, 52
Mohan, N., & Rafferty, D. 2015, PyBDSF: Python Blob Detection and Source Finder, Astrophysics Source Code Library, ascl:1502.007
Nayana, A. J., & Chandra, P. 2018, ATel, 11950, 1
Nayana, A. J., & Chandra, P. 2021, ApJL, 912, L9
Ofek, E. O., Rabinak, I., Neill, J. D., et al. 2010, ApJ, 724, 1396
Offringa, A. R., McKinley, B., Hurley-Walker, N., et al. 2014, MNRAS, 444, 606
Offringa, A. R., & Smirnov, O. 2017, MNRAS, 471, 301
Perley, D. A., Fremling, C., Sollerman, J., et al. 2020, ApJ, 904, 35
Perley, D. A., Ho, A. Y. Q., Yao, Y., et al. 2021, MNRAS, 508, 5138
Perley, D. A., Mazzali, P. A., Yan, L., et al. 2019, MNRAS, 484, 1031
Perrott, Y. C., Scaife, A. M. M., Green, D. A., et al. 2013, MNRAS, 429, 3330
Poznanski, D., Chornock, R., Nugent, P. E., et al. 2010, Sci, 327, 58
Prentice, S. J., Maguire, K., Smartt, S. J., et al. 2018, ApJ, 865, L3
Pursiainen, M., Childress, M., Smith, M., et al. 2018, MNRAS, 481, 894
Remillard, R. A., & McClintock, J. E. 2006, ARA&A, 44, 49
Rest, A., Garnavich, P. M., Khatami, D., et al. 2018, NatAs, 2, 307
Rivera Sandoval, L. E., Maccarone, T. J., Corsi, A., et al. 2018, MNRAS, 480, L146
Romero, C. E., Sievers, J., Ghirardini, V., et al. 2020, ApJ, 891, 90
Sault, R. J., Teuben, P. J., & Wright, M. C. H. 1995, in ASP Conf. Ser. 77, Astronomical Data Analysis Software and Systems IV, ed. R. A. Shaw, H. E. Payne, & J. J. E. Hayes (San Fransisco, CA: ASP), 433
Smirnov, O. M., & Tasse, C. 2015, MNRAS, 449, 2668
Tampo, Y., Tanaka, M., Maeda, K., et al. 2020, ApJ, 894, 27
Tanaka, M., Tominaga, N., Morokuma, T., et al. 2016, ApJ, 819, 5
Tasse, C. 2014, A&A, 566, A127
Tasse, C., Hugo, B., Mirmont, M., et al. 2018, A&A, 611, A87
Vinkó, J., Yuan, F., Quimby, R. M., et al. 2015, ApJ, 798, 12
Vurm, I., & Metzger, B. D. 2021, ApJ, 917, 77
Weiler, K. W., Panagia, N., Montes, M. J., & Sramek, R. A. 2002, ARA&A, 40, 387
Wilson, W. E., Ferris, R. H., Axtens, P., et al. 2011, MNRAS, 416, 832
Zwart, J. T. L., Barker, R. W., Biddulph, P., et al. 2008, MNRAS, 391, 1545